AGU PUBLICATIONS

JGR

Journal of Geophysical Research: Space Physics

RESEARCH ARTICLE

10.1002/2016JA022784

Key Points:
- Quantitative analysis of the IMF impacts on the OCB location
- The dawn-dusk asymmetry of OCB changes with IMF conditions
- MHD model predictions of OCB locations agree with the observations

Correspondence to:
C. Wang,
cw@spaceweather.ac.cn

Citation:
Wang, C., J. Y. Wang, R. E. Lopez, L. Q. Zhang, B. B. Tang, T. R. Sun, and H. Li (2016), Effects of the interplanetary magnetic field on the location of the open-closed field line boundary, *J. Geophys. Res. Space Physics*, *121*, doi:10.1002/2016JA022784.

Received 1 APR 2016
Accepted 11 JUN 2016
Accepted article online 24 JUN 2016

Effects of the interplanetary magnetic field on the location of the open-closed field line boundary

C. Wang[1], J. Y. Wang[1,2], R. E. Lopez[3], L. Q. Zhang[1], B. B. Tang[1], T. R. Sun[1], and H. Li[1]

[1]State Key Laboratory of Space Weather, National Space Science Center, Chinese Academy of Sciences, Beijing, China, [2]College of Earth Science, University of Chinese Academy of Sciences, Beijing, China, [3]Department of Physics, University of Texas at Arlington, Arlington, Texas, USA

Abstract Using global magnetohydrodynamic(MHD) simulation, we investigate the effect of the interplanetary magnetic field (IMF) on the location of the open-closed field line boundary(OCB), in particular the duskside and dawnside OCB and their asymmetry. We first model the typical OCB-crossing events on 22 October 2001 and 24 October 2002 observed by DMSP. The MHD model presents a good estimate of OCB location under quasi-steady magnetospheric conditions. We then systemically study the location of the OCB under different IMF conditions. The model results show that the dawnside and duskside OCBs respond differently to IMF conditions when B_Y is present. An empirical expression describing the relationship between the OCB latitudes and IMF conditions has been obtained. It is found that the IMF conditions play an important role in determining the dawn-dusk OCB asymmetry, which is due to the magnetic reconnection at the dayside magnetopause. The differences between the dawn and dusk OCB latitudes from MHD predictions are in good agreement with the observations.

1. Introduction

The open-closed field line boundary(OCB) is the interface between geomagnetic field lines that are open to solar wind and closed onto the opposite hemisphere [e.g., *Lockwood*, 1998; *Rae et al.*, 2004; *Kabin et al.*, 2004]. The location of the OCB connects closely to the most important dynamic processes in the Earth's magnetosphere, such as the large-scale magnetosphere convection and magnetic reconnection at the magnetopause/magnetotail [e.g., *Siscoe and Huang*, 1985; *Hubert et al.*, 2006; *Lester et al.*, 2007; *Milan et al.*, 2009; *Milan*, 2009; *Aikio et al.*, 2013; *Longden et al.*, 2014]. The study of shape and location of the OCB is not only important to estimate the total open magnetic flux which is a fundamental indicator of the total magnetic energy in the solar wind-magnetosphere-ionosphere coupling system but also to provide information of the magnetic reconnection location and rate.

According to *Dungey* [1961], magnetic reconnection takes place between the interplanetary magnetic field(IMF) and closed geomagnetic field lines on the dayside magnetopause when the IMF has a southward component. It causes part of the closed flux to be open and the area of polar cap to increase. New open flux tubes transfer from the dayside to the nightside under the drag of the solar wind, causing the magnetotail current sheet to thin. Eventually, the current sheet is sufficiently thin to be unstable to the onset of reconnection, which causes a decrease in the polar cap area once lobe flux begins to reconnect. Hence, the location of the OCB is substantially under the control of the magnetic reconnections at the magnetopause/magnetotail.

In the past years, great efforts have been paid to identify methods for determining the location of the OCB observationally. Determining the poleward edge of high-energy (1–10 s keV) electron precipitation a proxy for the OCB is considered as the most reliable method [e.g., *Lopez et al.*, 1991; *Newell et al.*, 1996; *Sotirelis et al.*, 1998, 2005]. This method is supported by the fact that high-energy electrons are trapped on the closed field lines, and the polar cap is either void or filled with polar rain. Ground-based optical photometers allow one to monitor continuously the OCB by determining the poleward border of 630 nm optical emissions [e.g., *Blanchard et al.*, 1995; *Johnsen and Lorentzen*, 2012]. *Blanchard et al.* [1997] went on to assess the validity of this method. They found that if identifying the OCB as 0.7° equatorward of the 110 Rayleigh transition of red line emissions, the error is less than $\pm 1.2°$ in the majority of cases. Using the data of Super Dual Auroral Radar Network (SuperDARN) coherent scatter radars, the OCB can also be identified by increasing spectral width of the reflected signal [*Chisham and Freeman*, 2003].

Satellite-based Imagers provide a useful method for defining the variation of the OCB over all local times and various solar wind conditions, especially during which substorm expansive phase activity took place [e.g., *Frank and Craven*, 1988; *Brittnacher et al.*, 1999; *Longden et al.*, 2010]. In these cases, the OCB position is identified with the polar edge of auroral glow. Another method is the magnetogram inversion technique [*Mishin*, 1990; *Kamide and Baumjohann*, 1993], which calculates electric potential, field-aligned current, and equivalent current using the long-period variable geomagnetic field in the polar region as input. In this method, the high-latitude boundary of Region-1 FAC is considered as the OCB [e.g., *Mishin et al.*, 2011, 2015]. In addition, the sophisticated MHD simulations can be used to describe the solar wind-magnetosphere interaction, thus can also make it possible to look at the character of the OCB in global scales [e.g., *Lopez et al.*, 1999; *Kabin et al.*, 2004; *Rae et al.*, 2004, 2010; *Wang et al.*, 2013a].

As would be expected, the location of the OCB is closely related to the orientations of IMF, which have significant impacts on the reconnections of magnetopause/magnetotail. Early work by *Holzworth and Meng* [1975] indicated that the radius of the OCB increases as B_Z become more negative, although for very strongly negative B_Z the amount of open flux saturates [*Lopez et al.*, 2009]. *Moses et al.* [1988, 1989] have suggested that observations might be consistent with departures from a nominally circular OCB. Based on the Dungey cycle, any imbalance between the dayside merging rate and nightside reconnection rate should lead to expansion and contraction of the polar cap, leading to the motions of the OCB [*Dungey*, 1961; *Milan et al.*, 2007]. Thus, the solar wind conditions which influence the reconnection rates should distort a nominally circular OCB and have significant effects on the location of the OCB. Taking advantage of the global MHD model, *Kabin et al.* [2004] have analyzed qualitatively the effects of changes in the IMF, dynamics pressure, and dipole tilt angle on the position of the OCB. One of the most important impact factors is the Y component of IMF. As the results of some previous studies, B_Y can lead to an asymmetry of the two-cell plasma convection pattern at the high-latitude ionosphere [e.g., *Heelis*, 1984; *Reiff and Burch*, 1985; *Heppner and Maynard*, 1987], thereby the asymmetry of the OCB [e.g., *Lee et al.*, 2010; *Lukianova and Kozlovsky*, 2011].

Recently, *Chen et al.* [2015] examined how the location of Convection Reversal Boundary(CRB) behaves as the orientation of IMF changes using DMSP observation data. They found that the boundary may deviate from a nominally circular shape due to the changes of IMF B_Z and B_Y. The CRB separates sunward plasma flow from antisunward plasma flow. Due to the viscous interaction, CRB should occur on closed magnetic field lines. Its latitude is close to but below the OCB. Comparisons of the OCB latitudes determined from particle precipitation to the CRB latitudes determined from SuperDARN observations have shown that on average, there is less than 1° of latitude at most magnetic local times between these two boundaries [*Sotirelis et al.*, 2005]. Since the DMSP observations are insufficient to describe the evolution of the boundary with great precision, Chen's work mainly focuses on the qualitative analysis.

The shape and location of the OCB is the important indicator of magnetic reconnection in the dayside magnetosphere/magnetotail, and their quantitative relationship with IMF has not yet been well understood. In this study, we will focus on the effect of IMF magnitude and orientation on the dawn-dusk OCB, especially any asymmetry, and try to obtain some quantitative results using a global MHD model. Section 2 will introduce the methodology including the Piecewise Parabolic Method with a Lagrangian Remap (PPMLR)-MHD model and the diagnosis methods to determine the location of the OCB. Section 3 will present the main results including two parts. The first part shows the comparison of the OCB between MHD simulations and DMSP observations. The second one is the numerical simulated study. Section 4 gives the discussions and summary.

2. Methodology

2.1. Global MHD Model

Taking advantage of the global 3-D MHD model, namely, Piecewise Parabolic Method with a Lagrangian Remap(PPMLR)-MHD model, we conduct a series of test runs under different solar wind and IMF conditions. The global PPMLR-MHD code [*Hu et al.*, 2005, 2007] is a solar wind-magnetosphere-ionosphere (SMI) coupling model, which is based on an extension of the Lagrangian version of the piecewise parabolic method developed by *Colella and Woodward* [1984] to MHD. The code has been well calibrated and successfully applied in modeling large-scale magnetospheric structures and various dynamical processes in the interaction of solar wind with the magnetosphere [*Wang et al.*, 2013b]. In this study, we use this code to solve the ideal MHD equations in GSM coordinates. The numerical mesh is set in a Cartesian coordinate system with the Earth centered at the origin and the X, Y, and Z axes pointing to the Sun, the dawn-dusk direction, and the north, respectively. The computational domain extends from $-300\ R_e$ to $30\ R_e$ along the X direction and from

$-150\ R_e$ to $150\ R_e$ along the Y and Z axes. Inside $-10\ R_e < X, Y, Z < 10R_e$, a uniform mesh is used with a grid spacing of 0.4 R_e; the grid spacing outside this region increases gradually along each axis with a geometrical series of common ratio 1.05. The total number of mesh points is $160 \times 162 \times 162$. An inner boundary is set at $r = 3\ R_e$ in order to avoid the complexity associated with the plasmasphere and strong magnetic field which will limit the time step of each run, and an electrostatic ionosphere is put at $r = 1.017\ R_e$ with uniform height-integrated conductance. A magnetosphere-ionosphere electrostatic coupling model is imbedded to drive the inner magnetospheric convection, which maps the field-aligned current $J_{\parallel}$ from the inner magnetospheric boundary to the ionosphere, and then maps the electric potential from the ionosphere to the inner boundary along the Earth's dipole field lines. For numerical details of this code, please refer to our previous work [*Hu et al.*, 2007]. Each run continues until a quasi-steady solution has been reached, which usually last more than 5 h in physical time. We then try to identify the interface between the open and close field lines from our simulation results.

2.2. Diagnosis Methods for the Open-Closed Field Line Boundary

As mentioned in section 1, several techniques exist for determining the location of the OCB, such as using global images of aurora, observations by SuperDARN radar, and particle measurements from polar-orbiting spacecraft. In this study, the whole OCB is defined from the global MHD simulation data. We trace all magnetic field lines from the footpoints at the inner boundary by using the Runge-Kutta method. The footpoint grid resolution is 1° in both magnetic longitude and latitude with the longitude varying from 0° to 360° and the latitude from 90° to 0°. An outer boundary is set to be $-80\ R_e < X < 20\ R_e$ and $-50\ R_e < Y, Z < 50\ R_e$ in an attempt to reduce the amount of calculations without losing generosity. The tracing process is stopped when the field line returns to the inner boundary of the magnetosphere, or it reaches the outer boundary or the total length exceeds 1000 R_e. If a field line finally reaches the inner boundary, it is then considered to be a closed field line; otherwise, it is assumed to be an open field line. We map all footpoints of field lines from the inner boundary to the ionosphere along the dipole field lines. The ionospheric grids connected to closed and open field lines are marked with −1 and 1, respectively. Since the OCB is the dividing line between the open and closed magnetic field region, the zero contour of those grids is our expected result.

3. Results

3.1. Comparison of the OCB Between MHD and DMSP Crossings

Before discussing the effect of IMF conditions on the location of the OCB, we would like first to check whether the OCB determined by the PPMLR-MHD approach matches the observations when the magnetosphere is in quasi-steady state. *Rae et al.* [2004] compared the OCB in the BATS-R-US MHD model to the poleward edges of CANOPUS photometer measurements of red line emission for nine events when interplanetary and ionospheric conditions were nearly constant for at least 2 h. They found that BATS-R-US may usually provide a good estimation for the actual location of the OCB under steady magnetospheric conditions.

In this study, we choose two typical OCB-crossing periods on 1130 UT – 1240 UT of 22 October 2001 and 1430 UT – 1500 UT of 24 October 2002 observed by the Defense Meteorological Satellite Program (DMSP) satellites, since these two periods have been used to study the open magnetic flux during sawtooth events in previous works [*Dejong et al.*, 2007; *Hubert et al.*, 2008]. The sawtooth event is driven by a long period of time of continuously southward and reasonably steady IMF [*Henderson*, 2004; *Henderson et al.*, 2006]. Both of these two periods occurred during one cycle of a specific sawtooth event. The first one occurred after the first onset (1106 UT) of the sawtooth event previously studied in *Dejong et al.* [2007]. The second period occurred after one onset(1400 UT) of the sawtooth event previously discussed by *Hubert et al.* [2008]. We can see from Figure 6 of *Dejong et al.* [2007] and Figure 2 of *Hubert et al.* [2008] that polar cap flux did not dramatically decrease or increase but basically remained steady during the above two periods. It implies that a dynamic balance existed between dayside merging and reconnection in the tail.

Under the solar wind conditions of the first period, the real magnetosphere can be approximately considered as a quasi-steady state with Pedersen conductance $\Sigma_p = 5\ S$, the solar wind velocity $v_{sw} = 580$ km/s, number density $n_{sw} = 5\ \text{cm}^{-3}$, and a southward IMF $B_Z = -10$ nT. During the second period, the real magnetosphere can be regarded to be a quasi-steady state with $\Sigma_p = 5\ S$, $v_{sw} = 650$ km/s, $n_{sw} = 7.5\ \text{cm}^{-3}$, and a southern IMF $B_Z = -5$ nT. For simplicity, we adopt the assumption of zero dipole tilt angle. *Kabin et al.* [2004] showed that a dipole tilt with the magnitude of 35°brings 1 – 2° deviation degree to the dawnside and duskside OCB. In Tables 1 and 2, we list the tilt angles when DMSP satellites cross the OCB. All tilt angles are below 10°. The

Table 1. A List of the DMSP Crossings During the Period on 22 October [a]

	Satellite	$\phi_{DMSP}(°)$	$\theta_{DMSP}(°)$	$\theta_{MHD}(°)$	$d\theta(°)$	$\Phi(°)$
UT 11:32	F14	294.52	−66.45	−68.33	1.88	−8.6
UT 11:44	F14	151.67	−70.61	−70.81	0.2	−8.1
UT 11:52	F13	280.11	−69.93	−68.67	−1.26	−7.8
UT 12:04	F13	95.07	−66.86	−69.36	2.5	−7.3
UT 12:22	F12	290.10	−68.48	−68.34	−0.14	−6.5
UT 12:35	F12	124.95	−67.29	−69.36	2.07	−6.0
Ave$d\theta$	–	–	–	–	0.87	–
Max$d\theta$	–	–	–	–	2.5	–

[a]Included in Table 1 are the UT, no. of satellite, the GSM longitude(ϕ_{DMSP}), and GSM latitude (θ_{DMSP}) of DMSP crossings, the corresponding OCB latitude from PPMLR simulation (θ_{MHD}), the deviations between DMSP determined and PPMLR-simulated OCB boundary ($d\theta = \theta_{DMSP} - \theta_{MHD}$), the average (Ave$d\theta$) and the maximum deviation (Max$d\theta$), and the dipole tilt angle (Φ). A negative latitude of DMSP crossings ($\theta_{DMSP} < 0$) illustrates that the satellite crosses OCB boundary at the Southern Hemisphere.

deviation degree due to the tilt angle is believed to be much smaller than the maximum of $d\theta$. We identify the OCB locations of these two MHD quasi-steady states using the diagnosis method introduced in section 2.2 and make comparisons between them and all DMSP boundary crossings during these two periods.

The DMSP satellites orbit the Earth in a Sun-synchronous 98° inclination orbit near 840 km altitude. Each satellite carries the Special Sensor Precipitating Electron and Ion Spectrometer sensor that measures the flux of precipitating ions or electrons between 30 eV and 30 keV once per second. There are data from three DMSP satellites (F12–F14) available during the above mentioned periods. Figure 1 shows an example of the boundary location identification procedures applied to a Southern Hemisphere pass of F13. Boundary crossings are determined by visual inspection of the flux and energy of precipitating ions and electrons [e.g., *Hardy*, 1984; *Sotirelis et al.*, 1998; *Milan et al.*, 2003]. The clearest boundary crossings are identified during generic southward IMF conditions when the cap is large and sometimes filled with polar rain. A sharp transition from precipitation characteristic of the plasma sheet to polar rain or void is a clear indication of the boundary, as marked by the vertical red lines in Figure 1.

Using this method, we determine 10 OCB crossings during these two time periods. The specific crossing events are listed in Tables 1 and 2. For the first period, the maximum deviation of OCB latitude between the MHD simulations and the DMSP observations is about 2.50°, and the average deviation is 0.87°. For the second period, the maximum deviation is about 1.93°, and the average is 0.57°. Figures 2a and 2b present the pattern of model-data comparison. The simulation results are in good agreement with the DMSP observations. We thus believe that the PPMLR-MHD code can reproduce the location of the OCB quite well under the steady IMF conditions and will use the model results to analyze the impact of IMF conditions on the shape and location of the OCB as follows.

3.2. Impact of IMF Conditions on the Dawnside and Duskside OCB

We discuss the simulated results for different IMF magnitude and orientation to analyze the influence of IMF conditions on the dawnside and duskside OCB, and particularly the asymmetry. The dawnside corresponds to

Table 2. A List of the DMSP Crossings During the Period on 24 October 2002[a]

	Satellite	$\phi_{DMSP}(°)$	$\theta_{DMSP}(°)$	$\theta_{MHD}(°)$	$d\theta(°)$	$\Phi(°)$
UT 14:30	F14	299.38	−72.49	−71.82	−0.67	−3.0
UT 14:41	F14	132.26	−68.46	−69.35	0.89	−2.7
UT 14:27	F13	284.93	−70.67	−70.82	0.15	−3.1
UT 14:39	F13	94.43	−67.44	−69.37	1.93	−2.8
Ave$d\theta$	–	–	–	–	0.57	–
Max$d\theta$	–	–	–	–	1.93	–

[a]Illustrations are the same as Table 1.

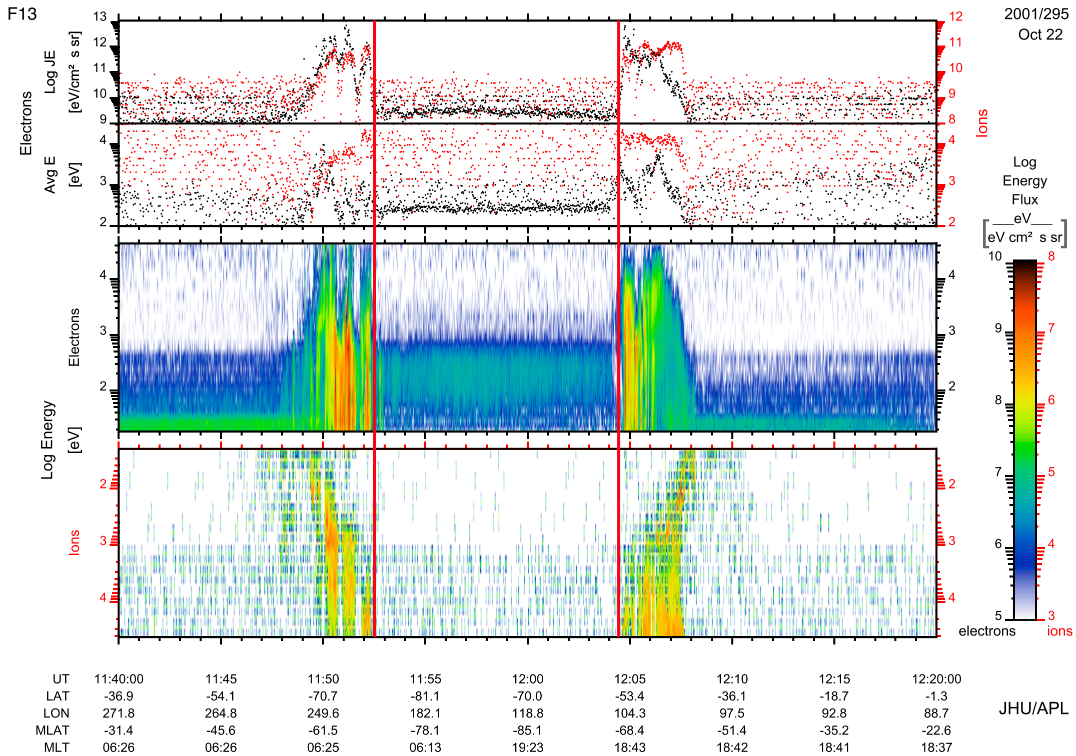

Figure 1. Electron and ion precipitation fluxes measured from DMSP F13 during the Southern Hemisphere pass on 22 October 2001. The first panel plots total energy flux in eV $\cdot$ cm^{-2} $\cdot$ s^{-1} $\cdot$ sr^{-1}, and the second panel shows average energy in eV; black refers to electron, red to ion. The spectrogram itself shows differential energy flux in units of cm^{-2} $\cdot$ s^{-1} $\cdot$ sr^{-1}. The actual open-closed boundary locations are marked by the vertical red lines.

6 magnetic local time (MLT), and the duskside corresponds to 18 MLT. We conducted a total of 76 numerical runs. For simplicity, we made the following assumptions.

1. The solar wind velocity is along the Sun-Earth line, and the Earth's dipole moment is due southward.
2. The solar wind velocity and number density are fixed to be 400 km/s and 5 cm^{-3}, and the ionospheric conductances are assumed to be uniform with a 5 S Pedersen conductance and a zero Hall conductance.

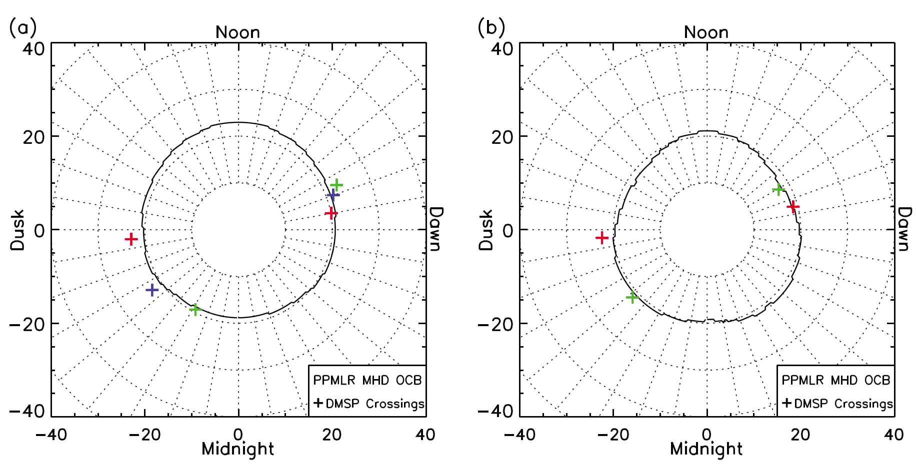

Figure 2. On the Southern Hemisphere, the pattern of comparison of latitudes between DMSP observations and PPMLR simulations; dotted circles represent 60°, 70°, and 80° MLAT. (a) Black solid line is the OCB location diagnosed from the PPMLR-MHD data under $\Sigma_p = 5$ *S*, $v_{sw} = 580$ km/s, $n_{sw} = 5$ cm^{-3}, and $B_Z = -10$ nT. (b) Black solid line is the OCB location of a quasi-steady state with $\Sigma_p = 5$ *S*, $v_{sw} = 650$ km/s, $n_{sw} = 7.5$ cm^{-3}, and $B_Z = -5$ nT. Crosses denote the DMSP OCB crossings; blue refers to F12 crossings, red to F13, and green to F14.

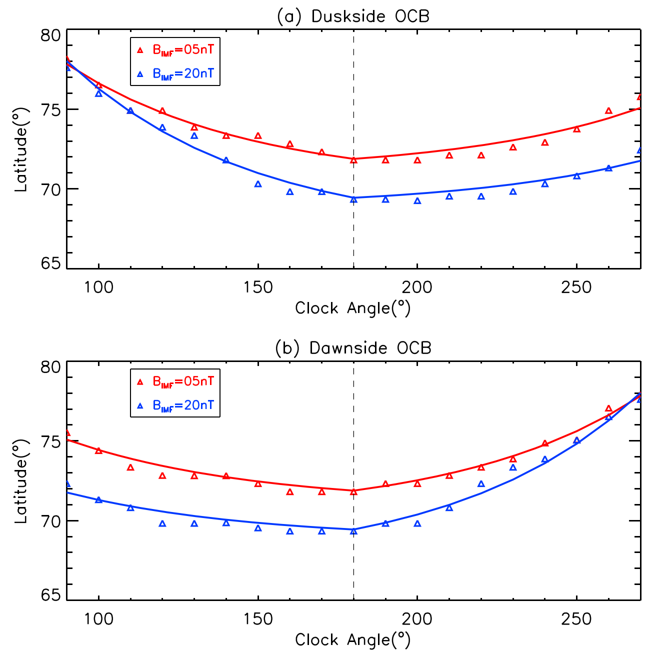

Figure 3. (a)The latitudes of the duskside OCB change with IMF conditions. (b) The latitudes of the dawnside OCB change with IMF conditions. The triangles denote the simulated results, and the solid lines are determined by equation (1) with the corresponding parameters being listed in Tables 3 and 4.

3. The IMF is perpendicular to the Sun-Earth line with adjustable magnetic strength B_{IMF} and clock angle θ_{CA}: $B_{\mathrm{IMF}} = 5, 10, 15, 20$ nT; $\theta_{\mathrm{CA}} = 90° \sim 270°$ (i.e., the IMF direction changes from duskward to dawnward with an interval of 10°).

In this study, we limit ourselves to a negative Z component ($B_Z < 0$), in which the SMI coupling is strong and sensitive to the magnitude and orientation of IMF. We focus on the dawnside and duskside OCB at the Northern Hemisphere. Due to the assumption of zero tilt angle, the Southern Hemisphere is antisymmetrically shaped with respect to the noon-midnight meridian.

The duskside and dawnside OCB latitudes change with IMF magnitude and orientation are plotted in Figures 3a and 3b, respectively. The red triangles denote the case for $B_{\mathrm{IMF}} = 5$ nT, and the blue triangles are for $B_{\mathrm{IMF}} = 20$ nT. As would be expected, the OCB expands with the increasing IMF magnitude with the blue triangles that are generally below the red triangles, indicating larger OCB oval. It is noted that the dawnside latitude is equal to the duskside latitude under due southward IMF conditions. We first consider the scenario under $B_Y > 0$ when the IMF clock angle θ_{CA} ranges from 90° to 180°. The OCB latitude decreases with the increasing IMF clock angle for both $B_{\mathrm{IMF}} = 5$ nT and $B_{\mathrm{IMF}} = 20$ nT. The duskside OCB latitude is higher than the dawnside, and the change in the duskside latitude for a given change in the IMF clock angle is bigger than the dawnside as well. The dependence of the duskside OCB latitude as a function of the IMF clock angle is larger for greater IMF magnitude; however, the dependence of the dawnside is not as strong. The opposite is just true for $B_Y < 0$ (θ_{CA} in the range from 180° to 270°). The OCB latitude increases with the increasing clock angle, and the duskside latitude is lower than the dawnside; the dependence of the duskside OCB latitude on the IMF clock angle is smaller than on the dawnside. As the IMF magnitude increases, the change dependence of the duskside OCB latitude is much smaller, while the dependence for the dawnside OCB latitude increases with growing IMF magnitude.

In an attempt to describe the above statement quantitatively, we try to find an empirical equation of the relationship between the OCB latitude and the IMF clock angle. The OCB latitude θ related to the dawn-dusk meridian could be expressed as follows in terms of the IMF clock angle θ_{CA}:

$$\theta = c_1 + c_2 \exp(|3.1416 - 0.0175\theta_{\mathrm{CA}}|) \tag{1}$$

where $c_1 + c_2$ represent the latitude for $\theta_{\mathrm{CA}} = 180°$ (no IMF B_Y); c_2 describes the dependence of the OCB latitude on the IMF clock angle. We apply the multiple parameters fitting to the simulated results and find the best

Table 3. The Fitting Parameters for the Duskside OCB Latitude Under $B_Y > 0$ and the Dawnside OCB Latitude Under $B_Y < 0$

B_{IMF} (nT)	c_1	c_2	RMSE
5	70.32	1.56	0.29
10	68.74	1.81	0.45
15	67.92	1.97	0.38
20	67.19	2.25	0.42

fit parameters under different IMF magnitude, which are listed in Tables 3 and 4. This nonlinear relationship between the OCB location and IMF as shown in Figure 3 discussed above can also be seen clearly from this empirical equation and its coefficients. For example, under a positive IMF B_Y, the dependence of the duskside OCB latitude on the IMF clock angle is higher for larger IMF magnitude, with the rate of 1.56 for $B_{\mathrm{IMF}} = 5$ nT to 2.25 $B_{\mathrm{IMF}} = 20$ nT. The solid lines in Figure 3 are determined by equation (1) with the corresponding coefficients. This empirical equation represents our simulated results quite well.

In addition to the dependence of the dawnside and duskside OCB on the IMF conditions, we also focus on the asymmetry between them. In order to study the asymmetry quantitatively, we describe the asymmetry between the dawnside and duskside OCB as follows:

$$Asy = \frac{|(90-\theta_{\mathrm{dawn}}) - (90-\theta_{\mathrm{dusk}})|}{(90-\theta_{\mathrm{dawn}}) + (90-\theta_{\mathrm{dusk}})} \times 100\% = \frac{|\theta_{\mathrm{dusk}} - \theta_{\mathrm{dawn}}|}{180 - (\theta_{\mathrm{dusk}} + \theta_{\mathrm{dawn}})} \times 100\% \tag{2}$$

where θ_{dawn} and θ_{dusk} are the latitudes of dawnside and duskside OCB, respectively. Figure 4 plots the asymmetry as a function of the IMF clock angle for two different IMF magnitudes. The extent of asymmetry for $B_{\mathrm{IMF}} = 5$ nT is indicated by the red triangles; the one for $B_{\mathrm{IMF}} = 20$ nT by the blue triangles. As shown in Figure 4, when IMF clock angle is 180° (due southward IMF case), the dawnside OCB has the same latitude as the duskside OCB, which is in fact symmetry. The extent of asymmetry decreases linearly with clock angle under IMF $B_Y > 0$ and increase linearly with clock angle in case of a negative IMF B_Y. This suggest the asymmetry becomes more significant as the IMF deviates far away from due southward. Once again, the relationship between the dawn-dusk asymmetry and the IMF clock angle could be described as

$$Asy = 0.0175 \cdot c_3 \cdot |180 - \theta_{\mathrm{CA}}| \tag{3}$$

The multiple parameters fitting to the simulated results have been applied, and the best fit parameters are listed in Table 5. The solid lines in Figure 4 are determined by equation (3) with the corresponding parameters. The fitting function represents our simulated results quite well. With the IMF magnitude increasing, both the extent of dawn-dusk asymmetry and its change rate as a function of the clock angle (i.e., c_3) increase.

It is always of interest to compare the model predictions with observations. Based on the Imager for Magnetopause-to-Aurora Global Exploration satellite measurement, *Lukianova and Kozlovsky* [2013] statistically estimated the OCB dynamics in different sectors of local time during two geomagnetic storms. Their results show that the OCB displacement along the dawn-dusk meridian depends on the IMF B_Y. During the main phase of the storm on 17–18 August 2001, the IMF B_Y changes from 5 to 20 nT and more. During this time the difference of the dusk-dawn latitudes for the OCB is 4.5° on the average, and the maximum can reach up to 6°–7°. In our simulated results, when $B_{\mathrm{IMF}} = 5, 10, 15, 20$ nT and $\theta_{\mathrm{CA}} = 90°$, the differences of the dusk-dawn latitudes ($\theta_{\mathrm{dusk}} - \theta_{\mathrm{dawn}}$) are 1.9°, 3.7°, 4.5°, and 5.5°, respectively, all falling within the range observed. This implies that our model predictions roughly agree with the observations.

Table 4. The Fitting Parameters for the Dawnside OCB Latitude Under $B_Y > 0$ and the Duskside OCB Latitude Under $B_Y < 0$

B_{IMF} (nT)	c_1	c_2	RMSE
5	71.04	0.84	0.40
10	69.89	0.66	0.40
15	69.25	0.64	0.24
20	68.83	0.61	0.37

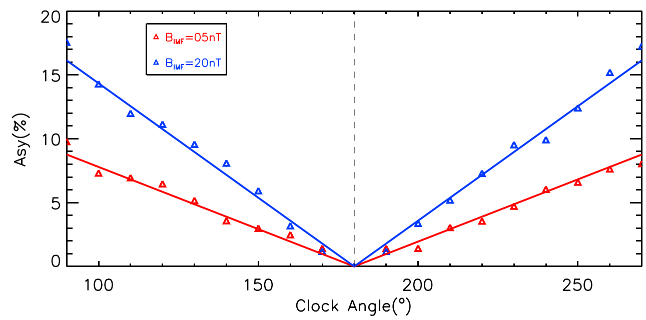

Figure 4. The dawn-dusk asymmetry changes with the IMF conditions. The triangles are calculated from the simulated results based on equation (2), and the solid lines are determined by equation (3) with the corresponding parameters being listed in Table 5.

4. Discussions and Summary

Using global MHD simulations, we have studied the effect of IMF conditions on the dawn-dusk OCB and their asymmetry. The OCB is controlled by magnetic reconnection in the magnetosphere, which is responsible for causing magnetospheric convection flows. The flow in the ionosphere is a marker of magnetospheric convection. Figure 5 presents the pattern of ionospheric plasma flows at the Northern Hemisphere for (a) $B_{IMF} = 5$ nT, $\theta_{CA} = 180°$ and (b) $B_{IMF} = 5$ nT, $\theta_{CA} = 120°$, respectively. When the Z component of the IMF is negative, and there is no Y component, dayside merging between the IMF and the Earth's field occurs near the equatorial plane; thus, the new open magnetic field lines are dragged toward high latitudes of the magnetotail across the two poles. Some open magnetic field lines are reconnected in tail, and new closed field lines are then flow toward dayside in low latitudes. Therefore, the ionospheric convection manifests a two symmetry cell convection pattern with antisunward flow across the polar cap and sunward flow at lower latitudes, as shown in Figure 5a. This is just the Dungey Cycle scenario. When the IMF has a positive(duskward) component in addition to the southward B_Z, the reconnection sites at the dayside magnetopause move from the equator to higher latitude of Northern Hemisphere at duskside and Southern Hemisphere at dawnside [*Park et al.*, 2006]. This causes a dawnward plasma flow in polar cap, and the duskside cell becomes more dominant than the dawnside [e.g., *Cowley et al.*, 1991; *Lukianova and Kozlovsky*, 2011], as shown in Figure 5b. The dawnward flow brings more open flux to dawnside; thus, the dawnside OCB has a lower latitude than duskside OCB at the Northern Hemisphere.

The general magnetospheric topological changes induced by constant IMF B_Y include the occurrence of an additional B_Y field in the tail having the same direction as IMF B_Y with a maximum value along the neutral sheet [e.g., *Lui*, 1986; *Borovsky et al.*, 1998] and the twisting of the tail and its current sheet [e.g., *Kaymaz et al.*, 1994, 1995; *Tsyganenko et al.*, 1998; *Walker et al.*, 1999]. Recently, *Wang et al.* [2014] analyzed the impact of IMF on the twisting of the magnetotail in terms of global PPMLR-MHD simulations. Their results showed that the cross sections of magnetotail are not rotationally symmetric but elongated along a certain direction. The elongated direction of the magnetotail and current sheet twists with the changing IMF clock angle. The relationship between the twisting angle and the clock angle is linear. This is the same as the relationship between the extent of asymmetry of the dawn-dusk OCB and the IMF clock angle. The magnetotail magnetopause twisting, current sheet twisting, and dawn-dusk OCB asymmetry are different phenomenon in different magnetospheric regions that all can be caused by the same source. That is when IMF has a B_Y component, the addition of new open flux tubes produced by dayside magnetic reconnection to the tail lobes has a dawn-dusk asymmetry about the noon-midnight meridian.

Table 5. The Parameters of Equation (3) Under Different IMF Magnitude

B_{IMF} (nT)	c_3	RMSE
5	5.59	0.51
10	6.44	0.75
15	8.05	0.47
20	10.27	0.77

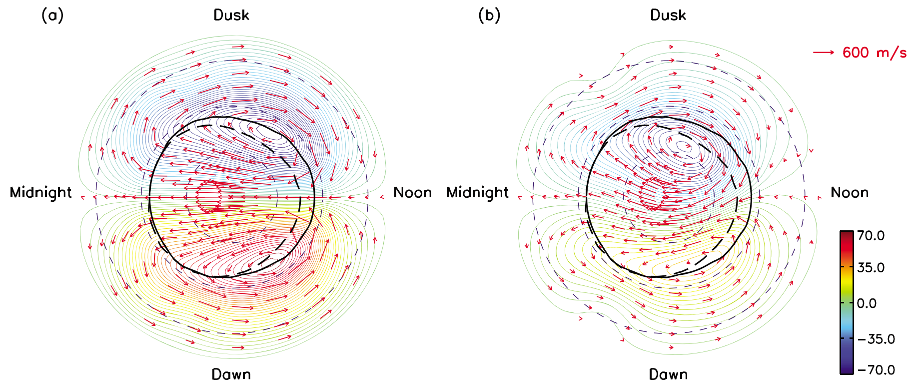

Figure 5. The pattern of ionospheric plasma convection flow at the Northern Hemisphere (a) under $B_{IMF} = 5$ nT, $\theta_{CA} = 180°$, (b) under $B_{IMF} = 5$ nT, $\theta_{CA} = 120°$; the background is ionospheric potential contour (in kV); red arrows indicate the direction of plasma convection flow; dashed circles represent 60°, 70°, and 80° MLAT; black solid lines are the OCB location under $B_{IMF} = 5$ nT, $\theta_{CA} = 180°$, and black dashed lines are under $B_{IMF} = 5$ nT, $\theta_{CA} = 120°$.

In this study, we use the simulated data with the IMF magnitude varying from 5 nT to 20 nT. With the IMF magnitude increasing, the OCB expands and the extent of dawn-dusk OCB asymmetry becomes significant. It is of interest to discuss the saturation effect for large IMF. Using our PPMLR-MHD model, *Wang et al.* [2013a] studied the impacts of interplanetary conditions on the open magnetic flux (F_{pc}) under the exclusively southward IMF. It is shown that the F_{pc} responds linearly to increases in the magnitude of B_Z initially. For larger values of B_Z (The interplanetary electric field is larger than 12 mV/m), the F_{pc} saturates. *Mitchell et al.* [2010] examined

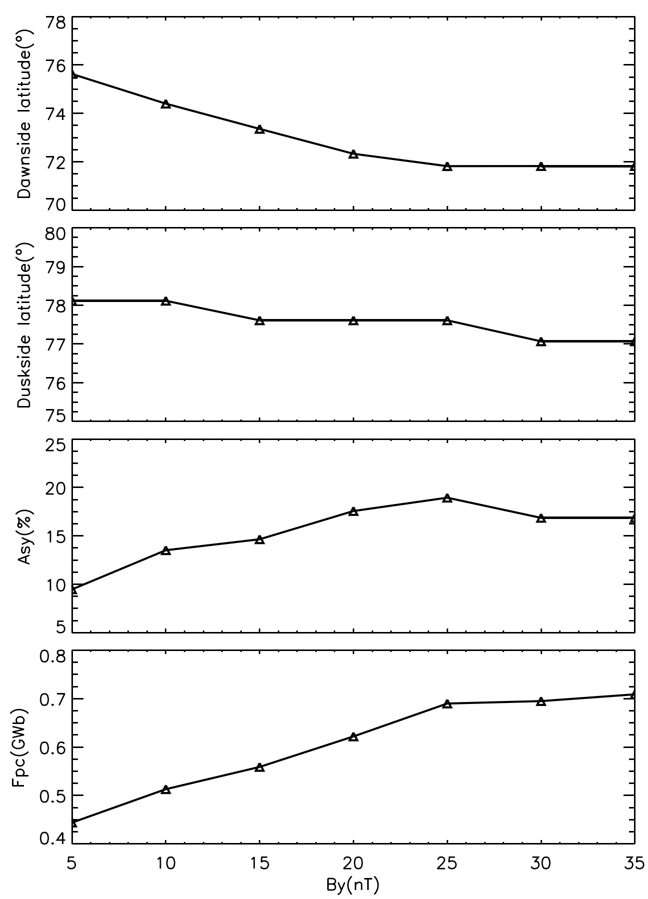

Figure 6. (top to the bottom) The dawnside OCB latitude, the duskside latitude, the asymmetry extent determined by equation (2), and the open magnetic flux change with IMF B_Y, respectively.

the response of the transpolar potential to a large IMF B_Y, and they found that the transpolar potential responds nonlinearly and saturates for large IMF B_Y based on the Lyon-Fedder-Mobarry global MHD simulation. It is thus reasonable to infer that the latitude of the OCB should also exhibit a similar signature for a large IMF. As shown in Figure 6, the OCB location and its asymmetry saturate for large IMF B_Y as the open magnetic flux (F_{pc}) does. The saturation region is above 25 nT. Nevertheless, the empirical equations (1) and (3) are appropriate for typical IMF conditions.

In summary, we first choose two typical OCB-crossing periods for adhering to the quasi-steady state picture and present the comparison of the OCB determined by DMSP measurements with those calculated from the global PPMLR-MHD model. During these intervals, we find good agreements between the model results and observations. Our MHD model captures the OCB location quite well when the magnetosphere is in a quasi-steady state. Then we use the model results to study the effect of IMF on the OCB locations, in particular the dawnside and duskside OCB latitudes and their asymmetry.

The OCB expands with the increasing IMF magnitude. Under a due southward IMF, the dawnside OCB has the same latitude as the duskside. When IMF B_Y is nonzero, the OCB has an obvious displacement along the dawn-dusk meridian. Based on our simulated data, we obtain two empirical expressions:

1. One describes the relation between the dawn-dusk OCB latitudes and the IMF conditions. In the case of $B_Y > 0$, the dawnside and duskside OCB latitudes decrease with the increasing IMF clock angle; for both the OCB latitudes and its dependence on the IMF clock angle, the duskside is bigger than the dawnside. When the IMF magnitude increases, the dependence of the dawnside OCB latitude remains almost constant, while the duskside increases. The opposite response is found for the dawnside and duskside OCB for $B_Y < 0$.
2. The other one describes the relation between the asymmetric extent and the IMF conditions. Like the twisting angle of magnetotail and current sheet, the extent of asymmetry of the dawn-dusk OCB has a linear relationship with the IMF clock angle. With the IMF magnitude increasing, the extent of asymmetry becomes significant. The deviated angle between the dawnside and duskside OCB latitudes from model predictions is in good agreement with the observations.

In this study, we just focus on the generic southward IMF cases ($B_Z < 0$). The effect of the northward IMF component on the location of the OCB will be conducted next. In addition, all data used in this study are obtained when the magnetosphere is in a quasi-steady state. We will try to model the OCB dynamics on a global scale during a specific substorm case as well in our future work.

Acknowledgments
This work was supported by the NNSFC grant 41231067, 973 program 2012CB825602, and in part by the Specialized Research Fund for State Key Laboratories of China. The OMNI data were generated by J.H. King and N. Papitashivilli and obtained from http://cdaweb.gsfc.nasa.gov/. The DMSP particle detectors were designed and calibrated by Dave Hardy, Fred Rich, and colleagues of AFRL, and data were provided via Applied Physics Laboratory at the Johns Hopkins University (JHU/APL) (http://sd-www.jhuapl.edu/Aurora/spectrogram/index.html). Numerical simulation data are available upon request from the corresponding author.

References

Aikio, A. T., T. Pitkänen, I. Honkonen, M. Palmroth, and O. Amm (2013), IMF effect on the polar cap contraction and expansion during a period of substorms, *Ann. Geophys.*, *31*(6), 1021–1034.

Blanchard, G. T., L. R. Lyons, J. C. Samson, and F. J. Rich (1995), Locating the polar cap boundary from observations of 6300 Å auroral emission, *J. Geophys. Res.*, *100*(A5), 7855–7862, doi:10.1029/94JA02631.

Blanchard, G. T., L. R. Lyons, and J. C. Samson (1997), Accuracy of using 6300 Å auroral emission to identify the magnetic separatrix on the nightside of Earth, *J. Geophys. Res.*, *102*(A5), 9697–9703, doi:10.1029/96JA04000.

Borovsky, J. E., M. F. Thomsen, and R. C. Elphic (1998), The driving of the plasma sheet by the solar wind, *J. Geophys. Res.*, *103*(A8), 17,617–17,639, doi:10.1029/97JA02986.

Brittnacher, M., M. Fillingim, G. Parks, G. Germany, and J. Spann (1999), Polar cap area and boundary motion during substorms, *J. Geophys. Res.*, *104*(A6), 12,251–12,262, doi:10.1029/1998JA900097.

Chen, Y.-J., R. A. Heelis, and J. A. Cumnock (2015), Response of the ionospheric convection reversal boundary at high latitudes to changes in the interplanetary magnetic field, *J. Geophys. Res. Space Physics*, *120*, 5022–5034, doi:10.1002/2015JA021024.

Chisham, G., and M. P. Freeman (2003), A technique for accurately determining the cusp-region polar cap boundary using SuperDARN HF radar measurements, *Ann. Geophys.*, *21*(4), 983–996.

Colella, P., and P. R. Woodward (1984), The Piecewise Parabolic Method (PPM) for gas-dynamical simulations, *J. Comput. Phys.*, *54*(1), 174–201, doi:10.1016/0021-9991(84)90143-8.

Cowley, S. W. H., J. P. Morelli, and M. Lockwood (1991), Dependence of convective flows and particle precipitation in the high-latitude dayside ionosphere on the X and Y components of the interplanetary magnetic field, *J. Geophys. Res.*, *96*(A4), 5557–5564, doi:10.1029/90JA02063.

Dejong, A. D., X. Cai, R. C. Clauer, and J. F. Spann (2007), Aurora and open magnetic flux during isolated substorms, sawteeth, and SMC events, *Ann. Geophys.*, *25*(8), 1865–1876.

Dungey, J. W. (1961), Interplanetary magnetic field and the auroral zones, *Phys. Rev. Lett.*, *6*(2), 47–48.

Frank, L. A., and J. D. Craven (1988), Imaging results from Dynamics Explorer 1, *Rev. Geophys.*, *26*(2), 249–283, doi:10.1029/RG026i002p00249.

Hardy, D. A. (1984), Precipitating electron and ion detectors (SSJ/4) for the block 5D/flights 6-10 DMSP satellites: Calibration and data presentation, Rep. AFGL-TR-84-0317, Air Force Geophysics Lab., Bedford, Mass.

Heelis, R. A. (1984), The effects of interplanetary magnetic field orientation on dayside high-latitude ionospheric convection, *J. Geophys. Res.*, *89*(A5), 2873–2880, doi:10.1029/JA089iA05p02873.

Henderson, M. G. (2004), The May 2-3, 1986 CDAW-9C interval: A sawtooth event, *Geophys. Res. Lett.*, *31*(11), L11804, doi:10.1029/2004GL019941.

Henderson, M. G., G. D. Reeves, R. Skoug, M. F. Thomsen, M. H. Denton, S. B. Mende, T. J. Immel, P. C. Brandt, and H. J. Singer (2006), Magnetospheric and auroral activity during the 18 April 2002 sawtooth event, *J. Geophys. Res.*, *111*, A01S90, doi:10.1029/2005JA011111.

Heppner, J. P., and N. C. Maynard (1987), Empirical high-latitude electric field models, *J. Geophys. Res.*, *92*(A5), 4467–4489, doi:10.1029/JA092iA05p04467.

Holzworth, R. H., and C.-I. Meng (1975), Mathematical representation of the auroral oval, *Geophys. Res. Lett.*, *2*(9), 377–380, doi:10.1029/GL002i009p00377.

Hu, Y. Q., X. C. Guo, G. Q. Li, C. Wang, and Z. H. Huang (2005), Oscillation of quasi-steady Earth's magnetosphere, *Chin. Phys. Lett.*, *22*(10), 2723–2726.

Hu, Y. Q., X. C. Guo, and C. Wang (2007), On the ionospheric and reconnection potentials of the Earth: Results from global MHD simulations, *J. Geophys. Res.*, *112*(A7), A07215, doi:10.1029/2006JA012145.

Hubert, B., S. E. Milan, A. Grocott, C. Blockx, S. Cowley, and J.-C. Gérard (2006), Dayside and nightside reconnection rates inferred from IMAGE FUV and Super Dual Auroral Radar Network data, *J. Geophys. Res.*, *111*, A03217, doi:10.1029/2005JA011140.

Hubert, B., S. E. Milan, A. Grocott, S. W. H. Cowley, and J. C. Gérard (2008), Open magnetic flux and magnetic flux closure during sawtooth events, *Geophys. Res. Lett.*, *35*, L23301, doi:10.1029/2008GL036374.

Johnsen, M. G., and D. A. Lorentzen (2012), A statistical analysis of the optical dayside open/closed field line boundary, *J. Geophys. Res.*, *117*, A02218, doi:10.1029/2011JA016984.

Kabin, K., R. Rankin, G. Rostoker, R. Marchand, I. J. Rae, A. J. Ridley, T. I. Gombosi, C. R. Clauer, and D. L. DeZeeuw (2004), Open-closed field line boundary position: A parametric study using an MHD model, *J. Geophys. Res.*, *109*, A05222, doi:10.1029/2003JA010168.

Kamide, Y., and W. Baumjohann (1993), *Magnetosphere-Ionosphere Coupling*, vol. 23, Springer, Berlin.

Kaymaz, Z., G. L. Siscoe, J. G. Luhmann, R. P. Lepping, and C. T. Russell (1994), Interplanetary magnetic field control of magnetotail magnetic field geometry: IMP 8 observations, *J. Geophys. Res.*, *99*(A6), 11,113–11,126, doi:10.1029/94JA00300.

Kaymaz, Z., G. Siscoe, J. G. Luhmann, J. A. Fedder, and J. G. Lyon (1995), Interplanetary magnetic field control of magnetotail field: IMP 8 data and MHD model compared, *J. Geophys. Res.*, *100*(A9), 17,163–17,172, doi:10.1029/95JA00593.

Lee, D.-Y., S. Ohtani, and J. H. Lee (2010), On the poleward boundary of the nightside auroral oval under northward interplanetary magnetic field conditions, *J. Geophys. Res.*, *115*, A08204, doi:10.1029/2009JA014906.

Lester, M., S. Milan, G. Provan, and J. Wild (2007), Review of ionospheric effects of solar wind magnetosphere coupling in the context of the expanding contracting polar cap boundary model, in *Solar Dynamics and Its Effects on the Heliosphere and Earth*, pp. 117–130, Springer, New York.

Lockwood, M. (1998), Identifying the open-closed field line boundary, in *Polar Cap Boundary Phenomena*, pp. 73–90, Springer, Netherlands.

Longden, N., G. Chisham, M. P. Freeman, G. A. Abel, and T. Sotirelis (2010), Estimating the location of the open-closed magnetic field line boundary from auroral images, *Ann. Geophys.*, *28*(9), 1659–1678.

Longden, N., G. Chisham, and M. P. Freeman (2014), Magnetic local time variation and scaling of poleward auroral boundary dynamics, *J. Geophys. Res. Space Physics*, *119*(12), 10,006–10,022, doi:10.1002/2014JA020430.

Lopez, R. E., H. E. Spence, and C.-I. Meng (1991), DMSP F7 observations of a substorm field-aligned current, *J. Geophys. Res.*, *96*(A11), 19,409–19,415, doi:10.1029/91JA01984.

Lopez, R. E., M. Wiltberger, J. G. Lyon, C. C. Goodrich, and K. Papadopoulos (1999), MHD simulations of the response of high-latitude potential patterns and polar cap boundaries to sudden southward turnings of the interplanetary magnetic field, *Geophys. Res. Lett.*, *26*(7), 967–970, doi:10.1029/1999GL900113.

Lopez, R. E., J. G. Lyon, E. Mitchell, R. Bruntz, V. G. Merkin, S. Brogl, F. Toffoletto, and M. Wiltberger (2009), Why doesn't the ring current injection rate saturate?, *J. Geophys. Res.*, *115*, A02204, doi:10.1029/2008JA013141.

Lui, A. (1986), Solar wind influence on magnetotail configuration and dynamics, in *Solar Wind Magnetosphere Coupling*, vol. 126, pp. 671–690, Terra Sci. Publ. Co., Pasadena, Calif.

Lukianova, R., and A. Kozlovsky (2011), IMF B_y effects in the plasma flow at the polar cap boundary, *Ann. Geophys.*, *29*(7), 1305–1315, doi:10.5194/angeo-29-1305-2011.

Lukianova, R., and A. Kozlovsky (2013), Dynamics of polar boundary of the auroral oval derived from the IMAGE satellite data, *Cosmic Res.*, *51*(1), 46–53, doi:10.1134/S0010952513010061.

Milan, S. E. (2009), Both solar wind-magnetosphere coupling and ring current intensity control of the size of the auroral oval, *Geophys. Res. Lett.*, *36*, L18101, doi:10.1029/2009GL039997.

Milan, S. E., M. Lester, S. W. H. Cowley, K. Oksavik, M. Brittnacher, R. A. Greenwald, G. Sofko, and J.-P. Villain (2003), Variations in the polar cap area during two substorm cycles, *Ann. Geophys.*, *21*(5), 1121–1140.

Milan, S. E., G. Provan, and B. Hubert (2007), Magnetic flux transport in the Dungey cycle: A survey of dayside and nightside reconnection rates, *J. Geophys. Res.*, *112*, A01209, doi:10.1029/2006JA011642.

Milan, S. E., J. Hutchinson, P. D. Boakes, and B. Hubert (2009), Influences on the radius of the auroral oval, *Ann. Geophys.*, *27*(7), 2913–2924, doi:10.5194/angeo-27-2913-2009.

Mishin, V., M. Förster, M. Kurikalova, and V. Mishin (2011), The generator system of field-aligned currents during the April 06, 2000, superstorm, *Adv. Space Res.*, *48*(7), 1172–1183, doi:10.1016/j.asr.2011.05.029.

Mishin, V., V. Mishin, S. Lunyushkin, Z. Pu, and C. Wang (2015), Strong induction effects during the substorm on 27 August 2001, *Earth Planets Space*, *67*(1), 1–10.

Mishin, V. M. (1990), The magnetogram inversion technique and some applications, *Space Sci. Rev.*, *53*(1), 83–163, doi:10.1007/BF00217429.

Mitchell, E. J., R. E. Lopez, R. J. Bruntz, M. Wiltberger, J. G. Lyon, R. C. Allen, S. J. Cockrell, and P. L. Whittlesey (2010), Saturation of transpolar potential for large Y component interplanetary magnetic field, *J. Geophys. Res.*, *115*, A06201, doi:10.1029/2009JA015119.

Moses, J. J., G. L. Siscoe, R. A. Heelis, and J. D. Winningham (1988), A model for multiple throat structures in the polar cap flow entry region, *J. Geophys. Res.*, *93*(A9), 9785–9790, doi:10.1029/JA093iA09p09785.

Moses, J. J., G. L. Siscoe, R. A. Heelis, and J. D. Winningham (1989), Polar cap deflation during magnetospheric substorms, *J. Geophys. Res.*, *94*(A4), 3785–3789, doi:10.1029/JA094iA04p03785.

Newell, P. T., Y. I. Feldstein, Y. I. Galperin, and C.-I. Meng (1996), Morphology of nightside precipitation, *J. Geophys. Res.*, *101*(A5), 10,737–10,748, doi:10.1029/95JA03516.

Park, K. S., T. Ogino, and R. J. Walker (2006), On the importance of antiparallel reconnection when the dipole tilt and IMF By are nonzero, *J. Geophys. Res.*, *111*, A05202, doi:10.1029/2004JA010972.

Rae, I. J., K. Kabin, R. Rankin, F. R. Fenrich, W. Liu, J. A. Wanliss, A. J. Ridley, T. I. Gombosi, and D. L. De Zeeuw (2004), Comparison of photometer and global MHD determination of the open-closed field line boundary, *J. Geophys. Res.*, *109*, A01204, doi:10.1029/2003JA009968.

Rae, I. J., et al. (2010), Comparison of the open-closed separatrix in a global magnetospheric simulation with observations: The role of the ring current, *J. Geophys. Res.*, *115*, A08216, doi:10.1029/2009JA015068.

Reiff, P. H., and J. L. Burch (1985), IMF By-dependent plasma flow and Birkeland currents in the dayside magnetosphere: 2. A global model for northward and southward IMF, *J. Geophys. Res.*, *90*(A2), 1595–1609, doi:10.1029/JA090iA02p01595.

Siscoe, G. L., and T. S. Huang (1985), Polar cap inflation and deflation, *J. Geophys. Res.*, *90*(A1), 543–547, doi:10.1029/JA090iA01p00543.

Sotirelis, T., P. T. Newell, and C.-I. Meng (1998), Shape of the open closed boundary of the polar cap as determined from observations of precipitating particles by up to four DMSP satellites, *J. Geophys. Res.*, *103*(A1), 399–406, doi:10.1029/97JA02437.

Sotirelis, T., J. M. Ruohoniemi, R. J. Barnes, P. T. Newell, R. A. Greenwald, J. P. Skura, and C.-I. Meng (2005), Comparison of SuperDARN radar boundaries with DMSP particle precipitation boundaries, *J. Geophys. Res.*, *110*, A06302, doi:10.1029/2004JA010732.

Tsyganenko, N. A., S. B. P. Karlsson, S. Kokubun, T. Yamamoto, A. J. Lazarus, K. W. Ogilvie, C. T. Russell, and J. A. Slavin (1998), Global configuration of the magnetotail current sheet as derived from Geotail, Wind, IMP 8 and ISEE 1/2 data, *J. Geophys. Res.*, *103*(A4), 6827–6841, doi:10.1029/97JA03621.

Walker, R., R. Richard, T. Ogino, and M. Ashour-Abdalla (1999), The response of the magnetotail to changes in the IMF orientation: The magnetotail's long memory, *Phys. Chem. Earth, Part C: Sol. Terr. Planet. Sci.*, *24*(1), 221–227.

Wang, C., Z. Y. Xia, Z. Peng, and Q. M. Lu (2013a), Estimating the open magnetic flux from the interplanetary and ionospheric conditions, *J. Geophys. Res. Space Physics*, *118*, 1899–1903, doi:10.1002/jgra.50255.

Wang, C., X. Guo, Z. Peng, B. Tang, T. Sun, W. Li, and Y. Hu (2013b), Magnetohydrodynamics (MHD) numerical simulations on the interaction of the solar wind with the magnetosphere: A review, *Sci. Chin. Earth Sci.*, *56*(7), 1141–1157, doi:10.1007/s11430-013-4608-3.

Wang, J. Y., C. Wang, Z. H. Huang, and T. R. Sun (2014), Effects of the interplanetary magnetic field on the twisting of the magnetotail: Global MHD results, *J. Geophys. Res. Space Physics*, *119*, 1887–1897, doi:10.1002/2013JA019257.